Materials Horizons

ROYAL SOCIETY OF CHEMISTRY

COMMUNICATION

View Article Online
View Journal

Cite this: DOI: 10.1039/d4mh00107a

Received 30th January 2024,
Accepted 15th March 2024

DOI: 10.1039/d4mh00107a

rsc.li/materials-horizons

Adaptive nanotube networks enabling omnidirectionally deformable electro-driven liquid crystal elastomers towards artificial muscles†

Jiao Wang,‡[ab] Hao Zhou,‡[a] Yangyang Fan,[ab] Wenhao Hou,[ab] Tonghui Zhao,[ab] Zhiming Hu,[ab] Enzheng Shi *[a] and Jiu-an Lv *[ab]

Artificial muscles that can convert electrical energy into mechanical energy promise broad scientific and technological applications. However, existing electro-driven artificial muscles have been plagued with problems that hinder their practical applications: large electro-mechanical attenuation during deformation, high-driving voltages, small actuation strain, and low power density. Here, we design and create novel electro-thermal-driven artificial muscles rationally composited by hierarchically structured carbon nanotube (HS-CNT) networks and liquid crystal elastomers (LCEs), which possess adaptive sandwiched nanotube networks with angulated-scissor-like microstructures, thus effectively addressing above problems. These HS-CNT/LCE artificial muscles demonstrate not only large strain (>40%), but also remarkable conductive robustness (R/R_0 < 1.03 under actuation), excellent Joule heating efficiency (≈ 233 °C at 4 V), and high load-bearing capacity (R/R_0 < 1.15 at 4000 times its weight loaded). In addition, our artificial muscles exhibit real-muscle-like morphing intelligence that enables preventing mechanical damage in response to excessively heavyweight loading. These high-performance artificial muscles uniquely combining omnidirectional stretchability, robust electrothermal actuation, low driving voltage, and powerful mechanical output would exert significant technological impacts on engineering applications such as soft robotics and wearable flexible electronics.

New concepts

Electro-driven artificial muscles exhibit broad availability and notable convenience for system control and integration. However, there are some problems that hinder their practical applications: large electro-mechanical attenuation during deformation, high-driving voltages, small actuation strain, and low power density. To solve the above problems, we created conceptually new hierarchically structured HS-CNT/LCE composite artificial muscles uniquely combining omni-directional stretchability, robust electrothermal actuation, low driving voltage, and powerful mechanical output. The as-prepared electro-driven artificial muscles show good lifting capacity, stable controllability and responsiveness characteristics. Importantly, a smart closed loop system that can enable autonomous and adaptive real-muscle-like intelligence is ingeniously constructed by the integration of electronic control components. The system's synchronous self-monitoring, self-alarming and self-healing capabilities provide great potential for closed-loop control. The engineering strategy disclosed herein could not only provide a general and practical method for manufacturing stable electro-driven artificial muscles, but also exert significant technological impacts on engineering applications such as soft robotics and wearable flexible electronics.

1. Introduction

Artificial muscles, which can undergo substantial deformation in response to various external stimuli, have received enormous attention in applications such as soft robotics, flexible electronics, and medical assist devices.[1,2] With the expanding demand for artificial muscles, a wide range of stimuli sources have been developed, including humidity,[3,4] electric field,[5] magnetic field,[6] light,[7,8] and heat,[9] and even multi-stimuli response.[10] Among various stimuli-driven artificial muscles, electrically powered artificial muscles that convert electrical energy into mechanical actuation provide many advantages for real engineering applications, such as the broad availability of electric energy input, and notable convenience for system control and integration.[11,12]

Many active soft materials have been developed as electro-driven artificial muscles, including ionic conducting polymers (*e.g.*, polypyrrole and polyaniline), non-ionic polymers (*e.g.*, dielectric elastomers, ferroelectric polymers, and electrostrictive polymers), ionic polymer–metal composites (IPMCs), and

[a] Key Laboratory of 3D Micro/Nano Fabrication and Characterization of Zhejiang Province, School of Engineering, Westlake University, Hangzhou, Zhejiang 310030, China. E-mail: lvjiuan@westlake.edu.cn, shienzheng@westlake.edu.cn

[b] Institute of Advanced Technology, Westlake Institute for Advanced Study, Hangzhou, Zhejiang 310024, China

† Electronic supplementary information (ESI) available. See DOI: https://doi.org/10.1039/d4mh00107a

‡ These authors contributed equally to the work.

electrically responsive gels (ERGs).[13] Ionic conducting polymers exhibit the advantages of low operation voltages, high actuation stress, and good biocompatibility. Their disadvantages include limited cycle life, high oxygen sensitivity, and restriction of working in aqueous solutions.[14] Non-ionic polymers feature fast response and large strain, and their salient limitation is the large activation field (typically > 10 MV m^{-1}) required for effective actuation, which often leads to the electrical breakdown of the materials.[15] IPMCs show various advantages, such as low driving voltages, high actuation strains, and micro/nanoscale manufacturing feasibility. Their limitations include low actuation bandwidth, small actuation stress, and short durability due to water leakage out of the surface electrode.[16,17] ERGs can offer the largest actuated change in volume, and their common drawbacks include heat/gas generation due to solution electrolysis, temperature/humidity-sensitive electromechanical response, and slow shape recovery.[18,19]

Liquid crystal elastomers (LCEs) have been increasingly considered as promising active soft materials for artificial muscles, because of their outstanding properties, including large and reversible actuation strains, tunable processability, and high programmability.[20–22] Three driving strategies have been mainly developed to enable electromechanical actuation for LCEs: (1) LCEs have worked as dielectric elastomer materials to generate large strains *via* electrostatic attraction.[23,24] Typically, a dielectric LCE actuator is fabricated by sandwiching a thin LCE film between two compliant electrodes. To enable electrostatic actuation, a high voltage of several kilovolts is applied to the two compliant electrodes to induce a strong electrostatic force that can generate a Maxwell stress contracting the sandwiched LCE film in thickness and expanding its area. The well-known advantage of dielectric elastomer actuation is their capability of high strains (up to 380%) and frequency (up to 500 Hz).[25,26] However, the notorious limitation of dielectric actuation is its high dependence on external high-voltage amplifiers that are usually large, bulk, and heavy, which greatly hinders the miniaturization, and integration of dielectric actuators for compact systems.[27] Moreover, excessive driving voltage ($\sim 10^2$ MV m^{-1}) inevitably brings safety issues during the actuation and operation.[28] (2) The electroclinic effect of ferroelectric LCEs has been explored for electromechanical actuation. This category of electromechanical actuation only needs an electric field of 1.5 MV m^{-1} (typically two orders of magnitude smaller than that required for dielectric elastomer actuation) to grant the actuation,[29] significantly reducing the needed intensity of the electric field. However, the generated actuation strain is much lower ($\sim 4\%$), while reported ferroelectric LCEs also exhibit a small modulus. The combination of relatively low actuation strains and a small modulus results in low work density.[30] (3) Joule-heating has been leveraged to gain electro-thermal-mechanical actuation in LCEs.[31–33] In this strategy, resistive elements (heaters) that can produce Joule heating, *e.g.*, metal wires, gold serpentine, liquid metals, and carbon nanoparticles, have been incorporated into and coupled with LCEs to realize electrothermal actuation through internally heating their composites to induce the phase transition from order to disorder of liquid crystals. The outstanding advantage of this strategy is that a low voltage of several volts (≤ 12 V) is high enough to power composited LCEs, which is safe and convenient for advanced real-world engineering applications. The great challenge for electrothermal LCEs is how to design and fabricate compliant heaters. For rigid metal heaters (*e.g.*, metal wires/thin films made of Ag, Au, Cu, *etc.*), stretchable structures (serpentine structures, spiral structures, and surface wrinkle structures) have been explored to endow rigid heaters with mechanical compliances. However, these stretchable structures usually only allow for specific single-direction compliance (*e.g.*, the longitudinal direction of a serpentine structure, and the axial direction of a spiral structure), while omnidirectional large deformations/stretching are prohibited otherwise they will damage the composited LCEs. Moreover, the introduction of hard metal structures inevitably enhances the rigidity of the composited LCEs and thus leads to a decrease in actuation strain and deformation rate.[34–36] Moreover, the substantial mismatch of intrinsic actuation strain between the rigid metal and LCE upon electrothermal actuation will yield stress concentration at their interfaces, leading to serious issues of stress-concentration-induced detaching. Soft heaters, such as liquid metals and carbon nanoparticles, allow for omnidirectional large deformations; however, the resistance R of such heaters will dynamically and significantly change during the deformation of LCEs, which unfortunately will result in unstable electro-thermo-mechanical output, because Joule-heating power P is directly related to the resistance, $P = V^2/R$ (where V is the driving voltage).

Through the analysis of the previous studies on electrically driven LCEs, we summarized four features of a high-performance electrically driven LCE actuator: (1) low driving voltage; (2) the introduced electrode material can deform concurrently with the driven LCE, and does not bring mechanical constraints to attenuate the shape-changing performance of the composited LCE; (3) the used electrode material allows for omnidirectional large-scale actuation/stretching; (4) stable electromechanical output during large deformation/stretching. If a novel electromechanical artificial muscle that combines the aforementioned features can be designed and created, this high-performance electrically driven artificial muscle would bring transformative impacts on the employment of LCEs in soft robotics and wearable technologies.

In this work, we judiciously devise omnidirectionally deformable electro-driven artificial muscles possessing adaptive sandwiched nanotube networks functioning *via* angulated-scissor-like microstructures, which enable the combination of the four features described above. Our artificial muscles exhibit superior conductive robustness ($R/R_0 < 1.03$ under 40% actuation), large actuation strain ($> 40\%$), high energy density (51 J kg^{-1}, more than twice that of human skeletal muscle), and large load-bearing capacity ($R/R_0 < 1.15$ at 4000 times its weight loaded). In addition, these high-performance electro-driven artificial muscles exhibit real-muscle-like intelligence of self-monitoring, self-alarming, and self-healing.

In contrast to previously reported electro-driven LCEs, we would like to highlight three outstanding advantages of HS-

CNT/LCE artificial muscles: (1) they exhibit unconventional capability to enable stable electro-thermo-mechanical output upon omnidirectional large deformation *via* adaptive sandwiched nanotube networks, which is critically important for precise electro-driven morphing control. (2) The use of self-assembled structured thin CNT films as compliant electrodes does not increase the stiffness of the artificial muscle component and maintains its large, rapid deformations. (3) Small driving voltages (<6 V) are enough to drive HS-CNT/LCE without the need for bulky high-voltage amplifiers/converters/powers. This advantage would not only eliminate the system's cost and size of the artificial muscles, but also make them compatible with conventional electronics and batteries, greatly facilitating system integration.

2. Results and discussion

Traditional electrothermal soft actuators have been troubled by fragile electrothermal components when subject to large deformations that lead to a notable decline in both electrical conductivity and electro-thermal efficiency. Moreover, the incorporation of a rigid electrothermal component could compromise the inherent flexibility of the soft actuator, thereby diminishing its capacity for actuation (Fig. 1a). We designed our high-performance electromechanical artificial muscles based on the aforementioned criteria, including low driving voltage, omnidirectional stretchability, and LCE's dominant deformation behaviors without mechanical constraints of the employed electrode materials.

To meet the first criterion, Joule-heating-driven actuation has been employed to gain low voltage (0–4 V) actuation for our electromechanical artificial muscles. The second criterion was satisfied through the rational design and fabrication of hierarchical structured CNT networks. Our electromechanical artificial muscles consist of two functional layers, one of which is the electro-driving layer composed of a hierarchical structured CNT network, responsible for stable electro-thermal conversion upon large deformation. The other layer is the mechanical actuation layer, which serves for stimuli-responsive deformation and mechanical output of the artificial muscle. This layer is made of a monodomain liquid crystal elastomer that offers large and reversible actuation. The electro-driving layer possesses a sandwich-like hierarchical structure (Fig. 1c). The upper layer and the lower layer of the sandwich-like structure consist of directionally aligned CNT networks, while the middle layer is composed of a randomly oriented CNT network. In comparison, for this sandwich-like hierarchical CNT structure, the layers of directionally aligned CNT networks can offer reversible stretching/deforming capability in the two orthogonal directions by changing the opening angle of angulated-scissor-like microstructures as well as the buckling/unbuckling

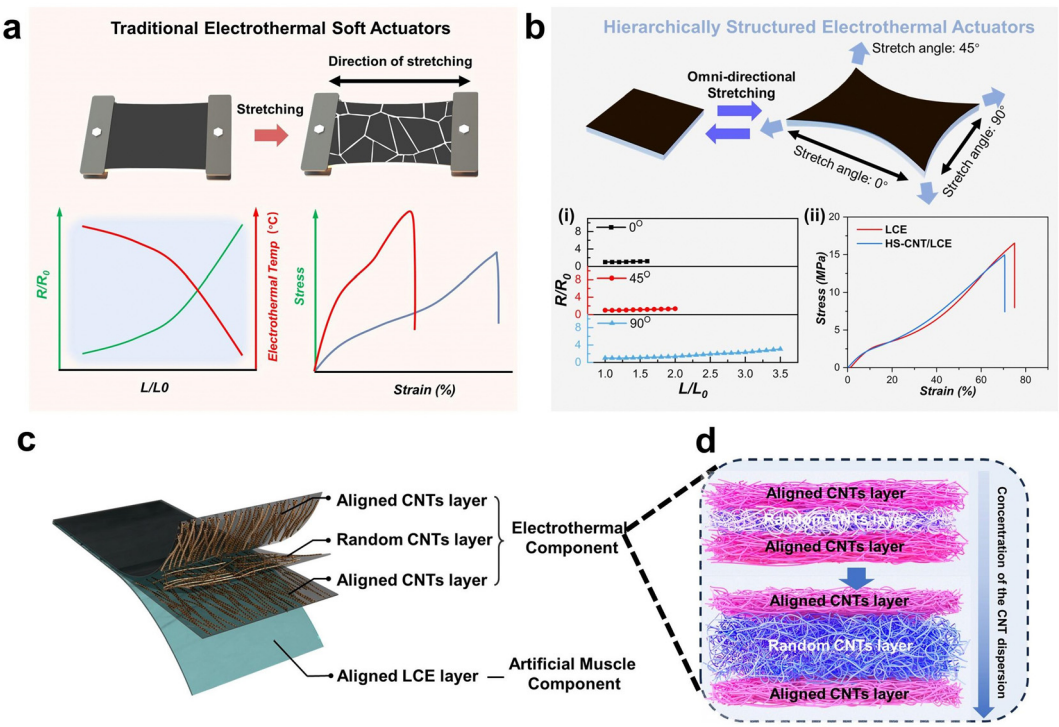

Fig. 1 The concept of omnidirectionally deformable electrothermal soft actuators. (a) Traditional electrothermal soft actuators showing poor conductive robustness, electrothermal stability, and deformation. (b) Schematic illustration of the deformation of our structured electrothermal soft actuators under applied forces. (i) Variation in resistance of a HS-CNT/LCE film under various stretch ratios and stretching angles (0°, 45°, and 90°). (ii) The strain/stress curve of the LCE film and HS-CNT/LCE film. (c) Schematic diagram of the HS-CNT film with a sandwiched structure including upper and lower aligned CNT layers and an intermediate random CNT layer. (d) The relative thickness of aligned and random CNT layers can be adjusted by raw CNT dispersion concentrations.

transition of CNTs. The middle layer of randomly oriented CNTs endows our artificial muscle with omnidirectional large-scale stretchability/deformation through reversible transformation between a randomly oriented CNT network and a directionally aligned CNT network. By actively and programmably changing the relative thickness of these three layers in the sandwich-like structure, we can achieve programmable modulation of direction-tunable stretchability of our artificial muscles without sacrificing electrothermal efficiency and mechanical actuation. Through taking advantage of adaptable angulated-scissor-like microstructures and dynamical buckling/unbuckling transition of CNTs, the microstructure-tunable artificial muscle can not only gain omnidirectionally stretchability, but also maintain good electro-thermal conversion under large deformation. As shown in Fig. 1b(i), the created HS-CNT/LCE artificial muscle possesses robust electrical stability and reliability under diverse stretching directions. To satisfy the last criterion, an ultrathin CNT electro-driving layer (2.96 μm in thickness, Fig. S7, ESI†) has been leveraged, which enables mechanical compliance with the deformation of the actuation layer. As shown in Fig. 1b(ii), two LCE actuators, one with the electrothermal drive layer while the other without, show similar strain–stress curves, which indicates that the introduction of the ultrathin hierarchical structured CNT network does not exert mechanical constraint on the actuation layer, thus avoiding the attenuation of electromechanical actuation.

The fabrication process of the HS-CNT/LCE film is depicted in Fig. S1 (see details of the preparation in the Method section, ESI†). First of all, the ultrathin HS-CNT film was prepared between two glass slides by the superacid sliding method.[37] The film thickness can be controlled by the SWCNT dispersion concentration and the force applied to spread the solution into a thin film (Fig. S2, ESI†). The alignment of CNTs within the HS-CNT is attributed to the shear forces arising from the interaction between the CNT dispersion and the glass slide during the superacid sliding process. The total thickness of the HS-CNT film exhibits a close correlation with the CNT raw dispersion concentration. As depicted in Fig. 1d, an increased concentration of the CNT dispersion results in a thicker film, diminishing the influence of shear forces and leading to an increase in the thickness of the random layers. Then we pre-stretched the loosely cross-linked LCE film and laminated the HS-CNT film on top of the LCE. The HS-CNT film can be well attached to LCE *via* the unreacted reactive groups on the loosely cross-linked LCE surface (Fig. S3, ESI†). Finally, the bilayer film undergoes stretching and ultraviolet (UV) irradiation to fix the alignment of the liquid crystal mesogens. The LCE film is responsible for generating a large actuating force and deformation, while the HS-CNT film provides Joule heating. By applying or removing an external voltage, the temperature of the LCE film can be controlled to generate reversible deformation. Increasing the voltage and elevating the temperature above the nematic–isotropic transition temperature (T_{NI}) of the LCE leads to a macroscopic shrinkage deformation, resulting in the contraction of the HS-CNT/LCE actuator. Upon removal of the voltage and cooling below T_{NI}, the LCE film returns to its original length. The glass transition temperature and T_{NI} of the LCE used in this study were −8.31 °C and 93.87 °C, respectively (as shown in Fig. S4, ESI†).

The HS-CNT films can retain their integrity during the transfer process due to the outstanding robustness and flexibility of CNTs as well as the clean interface between neighboring CNTs during the superacid process. By varying the concentration of the superacid dispersion, two types of HS-CNT films with distinct thicknesses were achieved, including CNT films fabricated from 4.7 mg mL^{-1} CNT dispersion solution and CNT films fabricated from 18.8 mg mL^{-1} CNT dispersion solution (Fig. S5, ESI†). At a lower concentration of the superacid dispersion (4.7 mg mL^{-1}), the ultrathin film displays higher optical transmittance and a larger sheet resistance of 156.3 Ω sq^{-1} (Fig. S6, ESI†). In comparison, as the concentration of the superacid dispersion increases to 18.8 mg mL^{-1}, the thickness of the films increases from ∼0.18 μm to ∼2.96 μm (Fig. S7, ESI†), and the electrical conductivity significantly increases, with a much lower sheet resistance of 3.1 Ω sq^{-1}. Meanwhile, the transmittance of the film decreases to below 5% (550 nm).

To demonstrate the reliability of the HS-CNT/LCE film, the resistance changes ($\Delta R/R_0$) of the omnidirectionally stretchable HS-CNT/LCE film were measured in multiple modes including bending, folding, twisting and stretching. The relative resistance changes of HS-CNT/LCE upon bending, folding, and twisting are shown in Fig. S8 (ESI†), which indicates that the resistance of the artificial muscles remains almost unchanged upon the three different deformations.

During the stretching process of these hybrid films, the CNTs generally exhibit two modes of behavior, orientation to the stretching direction without sliding and sliding between each other. The focus of maintaining electrical stability during stretching is to minimize the sliding between inter-connected individual CNTs. The HS-CNT films are composed of two aligned CNT layers and a relatively thin random layer. As shown in Fig. S9–S11 (ESI†), when stretched along the shearing direction (0°), there would be apparent sliding between neighboring CNTs due to the high degree of orientation, leading to high-density cracks within the HS-CNT film (prepared from 4.7 mg mL^{-1} dispersion) after a certain stretching ratio and resulting in a dramatic increase in the resistance. When the stretching direction is rotated by 90° (perpendicular to the shearing direction), the CNTs will be reoriented to the stretching direction by opening the closed angulated scissor-like micro-architectures, thus stabilizing without large fluctuation. In comparison to the >25 times resistance increase when the stretching direction is parallel to the shearing direction (60% strain), the resistance increase is controlled as low as ∼60% when the stretching direction is rotated by 90°. To further optimize the electrical stability during the stretching cycles, the concentration of the superacid dispersion was increased to 18.8 mg mL^{-1}. In the corresponding thick CNT film, the random CNT layer began to dominate. As shown in Fig. 2a, the CNTs of the random layer reoriented along the stretching

direction after 100% of stretching, in which the degree of sliding between CNTs is lower compared to that in the pre-aligned CNT layer. Consequently, the thick HS-CNT film (18.8 mg mL^{-1}) can dissipate the deformation energy more efficiently, thus reducing the negative effects of mechanical stretching on the electrical properties of the hybrid film.

The resistance changes of the HS-CNT/LCE films and commercialized conductive films are depicted in Fig. 2b. It was noted that the commercialized conductive films and HS-CNT film (4.7 mg mL^{-1}) exhibited a significant increase in resistance due to its fracture upon stretching. Notably, the commercialized conductive films became insulating under an applied strain of $<50\%$. For a thick HS-CNT film (18.8 mg mL^{-1}), the increase in resistance was significantly reduced. The relative change in resistance of the HS-CNT film (18.8 mg mL^{-1}) remained below 20% even at a large stretching ratio of 60% (L/L_0 = 1.6). Fig. 2c and Fig. S12 (ESI†) show the measured resistance change R/R_0 as a function of the strain at stretching angles of 0° and 90°, respectively. The resistance remained essentially stable ($R/R_0 < 1.03$) if the stretching ratio of the HS-CNT/LCE actuator was less than 20% ($L/L_0 < 1.2$), corresponding to the reorientation process of CNTs described above. Once it was recovered to its original state, the resistance of the HS-CNT film returned to its original value, indicating that the HS-CNT film could be stretched by 1.2 times without damage. If the stretching ratio was beyond 1.2, the resistance slightly increased, which was caused by the gradual sliding between the CNTs. The resistance increases during the loading and reversibly decreases during unloading, forming a hysteresis loop. The following loading/unloading cycles with the same stretching ratio can generate identical resistance–strain behavior, which is consistent with previous studies.[38] Fig. 2d presents the resistance change of the thick HS-CNT film for 1500 reversible stretch cycles. The HS-CNT film displayed excellent cyclic stability, and the degree of resistance change remained at a low level ($R/R_0 \leq 1.2$) throughout the whole process.

The actuating performance of the HS-CNT/LCE actuator is primarily determined by the characteristics of the electrothermal

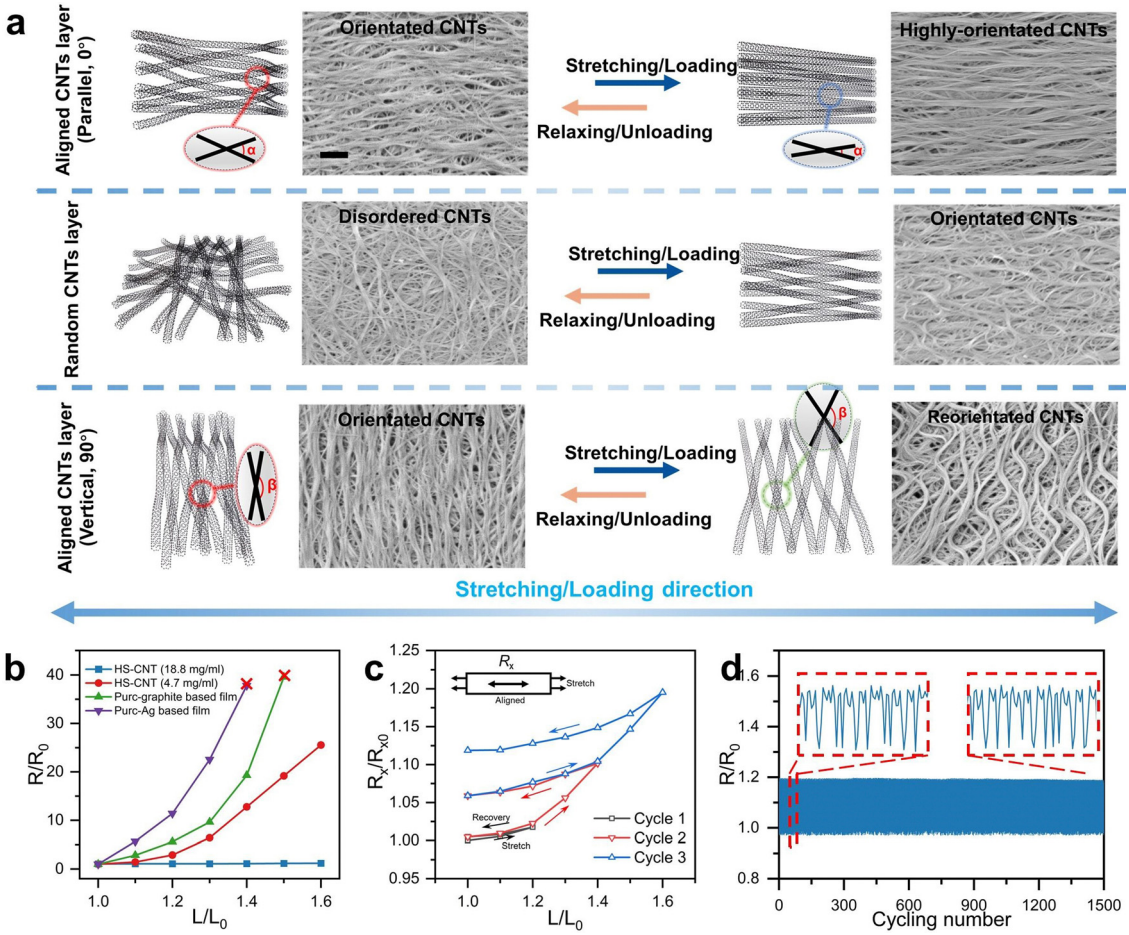

Fig. 2 Characterization of thick HS-CNT films. (a) The schematics and SEM images showing the evolution of the aligned and random CNT layers before and after 100% stretching (L/L_0 = 2) along different directions (0° and 90° to the shearing direction). Scale bar is 400 nm. (b) Variation in resistance of the thin and thick HS-CNT films (fabricated from 4.7 mg mL^{-1} and 18.8 mg mL^{-1} CNT dispersion solution), commercialized conductive graphite-based and Ag-based films under various stretching ratios. (c) Resistance changes as a function of strain under a cyclical loading. These three plots represent the experimental results of the resistance change along the shearing direction under three sequentially loading cycles (cycle 1 → cycle 3). (d) Variation in resistance of the thick HS-CNT film for 1500 stretching cycles along the shearing direction (L/L_0 = 2).

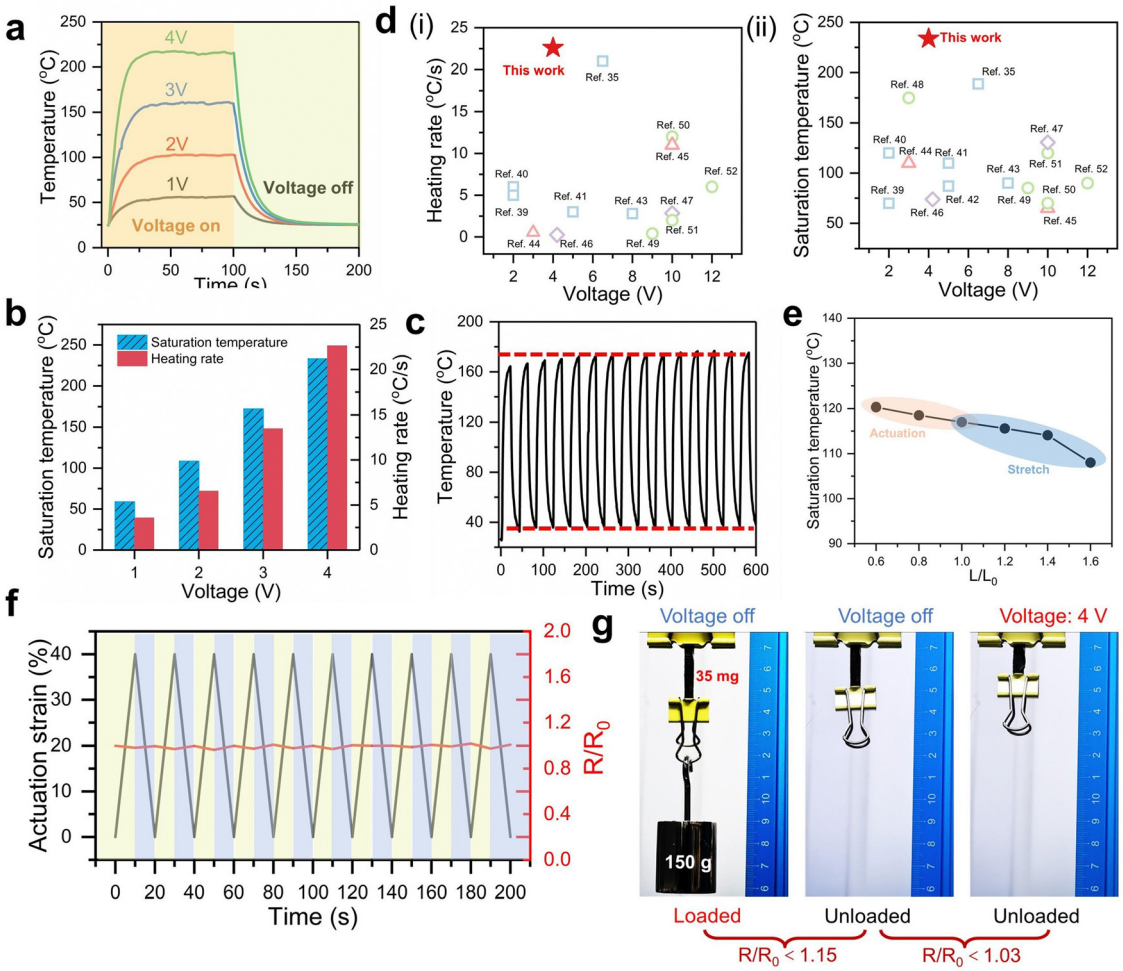

Fig. 3 Characterization of electrothermal and mechanical performance of the bilayer HS-CNT/LCE actuator. (a) The time-dependent temperature profiles of the bilayer under different applied voltages. (b) The heating rate and saturation temperature under different applied voltages. (c) Cyclic variation of temperature under an applied or removed voltage of 3 V. (d) Comparison of heating rates (i) and saturation temperatures (ii) of flexible electrothermal films, including Ag-based heaters, carbon-based heaters, Mxene-based heaters conductive polymer heaters, and the HS-CNT heater of this work under a low voltage. (e) Temperature distribution of the HS-CNT/LCE actuator during the actuation process and stretching process. (f) The actuation strain and corresponding resistance change during reversible thermal actuation of 10 cycles. (g) Experimental photographs of a HS-CNT/LCE actuator loading a 150 g weight (left) and the reversible contraction under on/off voltage (4 V) without loading (right). The resistance remains stable throughout the whole process.

HS-CNT film, including temperature distribution under different conditions, heating rates, and saturation temperatures. Fig. 3a illustrates the variation of temperature profiles of the HS-CNT/LCE film over time with applied voltages of 1, 2, 3, and 4 V. The results indicate that the rise time remains constant regardless of the voltage, while the saturation temperature is directly proportional to the applied voltage. Additionally, the relationship between the heating rate and saturation temperature under varying voltage inputs is presented in Fig. 3b. The heating rate is defined as the ratio of temperature change to response time, and the results indicate that both the heating rate and saturation temperature increase with the increase of applied voltage. The saturation temperature reaches approximately 233 °C with a heating rate of 22 °C s^{-1} at 4 V, which is consistent with the equation $P = V^2/R$ and elevated voltages tend to be accompanied by high heating rates and high saturation temperatures.

Fig. 3c presents the thermal stability and durability of the HS-CNT/LCE actuator, which underwent 15 cycles at 3 V. The heating performance remained consistent even during the 10-minute cycle test. For comparison purposes, the saturation temperature and heating rate of various electrothermal films under low voltage ($\leq$12 V), including Ag-based heaters,[35,39–43] Mxene-based heaters,[44,45] conductive polymer heaters,[46,47] carbon-based heaters,[48–52] and the HS-CNT heater proposed in this study were evaluated, as depicted in Fig. 3d(i and ii). The results indicate that the saturation temperature and heating rate of the HS-CNT film exceeded those reported in previous studies for electrothermal films under low voltage due to the high conductivity of HS-CNT films. The comparison highlights once again the advantage of the HS-CNT/LCE actuator. The uniform temperature distribution in different processes, including bending and stretching, facilitated consistent and

stable Joule heating for precise deformation control of the HS-CNT/LCE actuator. As shown in Fig. 3e, the HS-CNT/LCE actuator presented a uniform temperature range of 26 °C to 117 °C without deformation at 2 V, and only an 8% reduction in the saturation temperature even when the stretching was 1.4. Furthermore, the saturation temperature only varies by less than 3% even at 40% of the actuation strain. Fig. 3f presents the actuation strain and resistance change of the HS-CNT/LCE actuator for 10 reversible thermal actuation cycles. The HS-CNT/LCE actuator demonstrates excellent thermal actuation performances, contracting and decreasing to 40% of its initial length as the temperature increases. The electrical conductivity remains nearly constant throughout the whole process. Fig. 3g demonstrates optical images of the HS-CNT/LCE film. When an electrical potential of 4 V was applied, the film contracted by 40% of its initial length (Movie S1, ESI†). The resistance of the film remains essentially constant throughout the actuation process ($R/R_0 < 1.03$). When a 150 g (4000 times its own weight) weight was loaded, the film was stretched further, causing the resistance to increase, but the degree of change remained at a low level ($R/R_0 < 1.15$). Based on these results, it can be concluded that reversible thermal actuation was achieved with HS-CNT/LCE actuators, demonstrating excellent and stable electrothermal capabilities.

A low-voltage-driven artificial muscle was generated through the reversible deformation of the HS-CNT/LCE actuator by controlling the external voltage. The actuation stress of the artificial muscle was evaluated by fixing both ends of the film to a uniaxial testing machine with a tensile force of 0.1 N. When the applied voltage was increased from 1 to 4 V at 1 V intervals and the heating time was kept constant at 20 s, the maximum actuating stress of the artificial muscle showed an almost linear increase, as illustrated in Fig. 4a. Moreover, the duration of the applied voltage also plays a role in determining the maximum actuating stress. As shown in Fig. 4b, at a fixed applied voltage of 4 V, increasing the duration of the applied voltage from 5 to 20 s resulted in higher actuation stresses. Notably, when the duration was extended to 20 s, the actuation stress of the artificial muscle reached 1.1 MPa, far surpassing that of mammalian skeletal muscles ($\sim$0.35 MPa) and previous electrically driven LCE actuators. As shown in Fig. S13 (ESI†), the actuation speed of the artificial muscle can be tuned from 0–41%/s by changing the intensity of the applied voltage. The performance of a soft artificial muscle was further evaluated in terms of its actuation and recovery time, as well as its weightlifting capability. The weightlifting capability of the artificial muscle was assessed by applying a constant load to the end of the LCE film and measuring the thermomechanical contraction force in response to an applied voltage of 4 V. The strain was calculated as the decrement in displacement (ΔL) relative to the reference length (L_0) before loading at room temperature. It was observed that the specific work, defined as work done per unit mass of artificial muscle (m = 130 mg), was nearly proportional to the mass of the loaded weight, reaching a maximum at 90 g (more than 700 times the actuator's weight), with the actuation strain gradually decaying (Fig. 4c and Fig. S14, ESI†). The maximum specific work done by the system was 51 J kg^{-1}, which is higher than those of most LCE artificial muscles and human skeletal muscles.[11,35]

We demonstrate that our HS-CNT/LCE artificial muscles can enable a wide range of motion patterns (Movie S2, ESI†). As depicted in Fig. 4d, a directionally arranged HS-CNT/LCE actuator was employed as an artificial masseter muscle. Upon applying a low voltage of 4 V, it exhibited rapid contraction, resulting in the closure of the jaw—an imitation of the biological function of biting. Furthermore, the actuator was fixed to the upper limbs of a skeletal model, acting as a biceps artificial muscle. Upon applying a low voltage of 4 V, the biceps artificial muscle contracted swiftly, causing the arm to bend at the elbow, effectively mimicking human action. Similarly, the composite artificial triceps femoris imitated the lifting movement of the calf. These remarkable demonstrations highlight the versatility of our HS-CNT/LCE actuators as artificial muscles, making them ideal for a broad range of applications, including flexible robots, wearable exoskeletons, and medical rehabilitation equipment.

The cyclic stability of artificial muscles driven by applying a voltage of 3 V at a frequency of 0.05 Hz was evaluated as shown in Fig. 4e. The artificial muscles displayed excellent cyclic stability with a stable actuation stress of over 6000 actuation cycles. These findings demonstrate the potential of the HS-CNT/LCE actuator as a low-voltage-driven artificial muscle. Another significant performance of the electrically driven soft artificial muscle is the synergistic effect of multiple actuators. As shown in Fig. 4f and Fig. S15 (ESI†), multi-stack actuators with 4 and 10 layers were fabricated. The results demonstrate that the weight-lifting capability of the artificial muscle can be significantly enhanced by stacking multiple muscles. When 10 layers of the artificial muscles were utilized in unison, a weight exceeding 1 kg was successfully lifted within 12 seconds (Movie S3, ESI†), a remarkable working capability that was previously unattainable with traditional thermally actuated and photo-actuated LCE artificial muscles. In general, the HS-CNT/LCE outperforms the previously reported studies, further demonstrating the successful preparation of high-performance electromechanical artificial muscles, including low-voltage driving, favorable actuation performance (stress, strain, and rate), omnidirectional stretchability and conductive robustness (Table S1, ESI†). These findings provide valuable support for the electrically driven soft artificial muscle and its potential applications.

The unique combination of HS-CNT/LCE films featuring electrothermal actuation and resistive-stretching properties enables a diverse range of control strategies. In this study, we demonstrate an artificial muscle system with the ability to autonomously alert and repair itself, inspired by the human behavior of lifting heavy objects (Fig. 5a), a seemingly simple behavior that undergoes complex neural regulation. When a muscle is subjected to the force of a heavy object, impulses are generated by the cerebral cortex, leading to the excitation of α and γ nerve fibers. The excitation triggers the contraction of both extrafusal and intrafusal muscle fibers. The contraction of

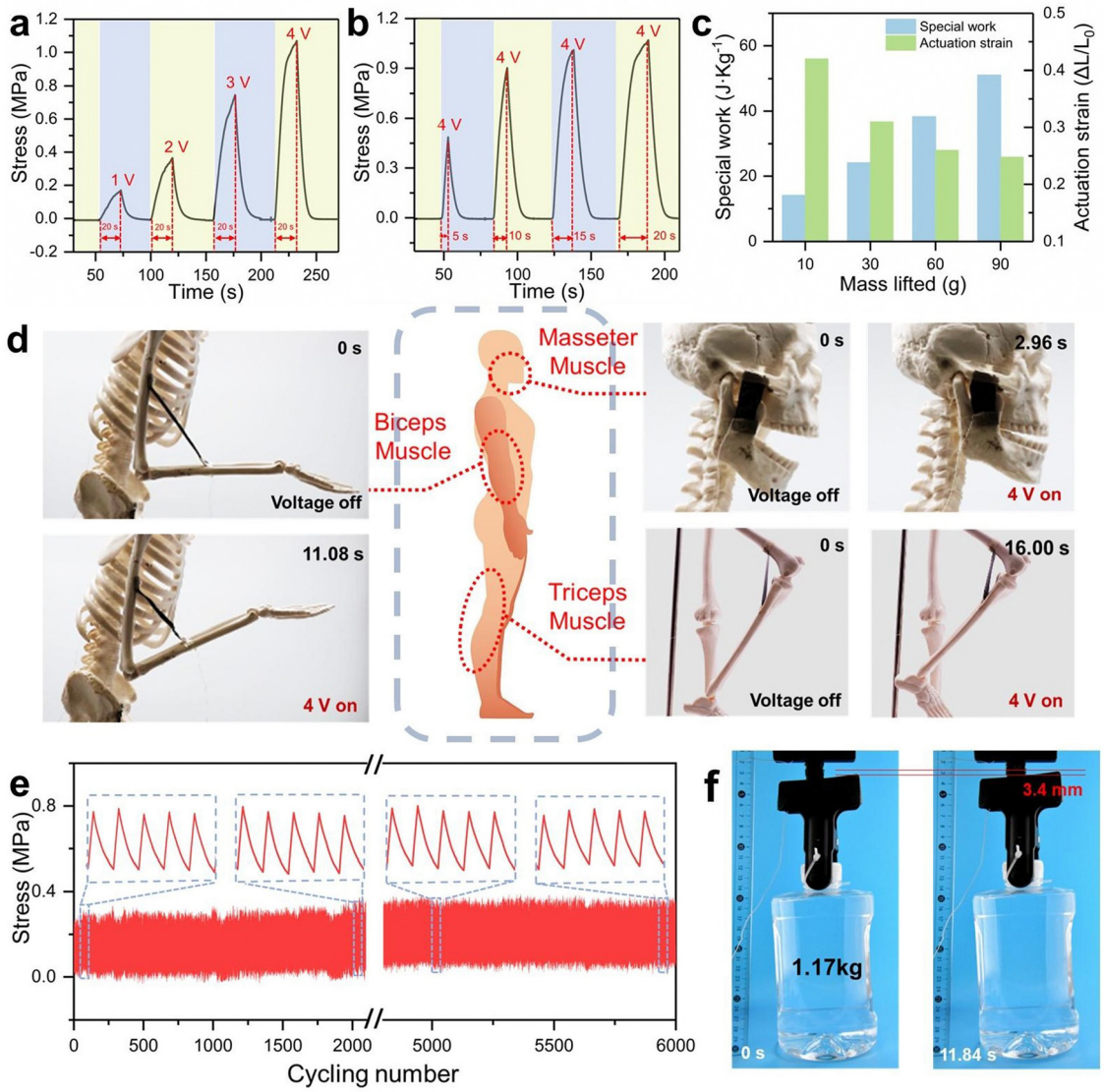

Fig. 4 Electrically controlled HS-CNT/LCE artificial muscle. Influences of the applied voltage (a) and heating time (b) on actuating stress generated in the HS-CNT/LCE artificial muscle. (c) Specific work and actuation strain of the HS-CNT/LCE actuator when lifting different weights. (d) Demonstration of the HS-CNT/LCE actuator served as masseter artificial muscle, biceps artificial muscle, and triceps artificial muscle. (e) Actuation stress during 6000 on/off voltage cycles (3 V, On 10 s; Off 10 s). (f) Multiple HS-CNT/LCE artificial muscles lifting 1.17 kg objects at a voltage of 4 V.

extrafusal muscle fibers, induced by the excitation of α neurons, opposes the applied force, while the contraction of intrafusal muscle fibers, caused by the excitation of γ neurons, maintains the afferent excitation of the muscle spindle. This ensures the strength of the myotatic reflex, allowing for the successful lifting of the weight. From the perspective of the structural composition of the reflex arc, the muscle spindle serves as not only a receptor, sensing the applied force and transmitting the signal to the brain, but also an effector, generating an appropriate force response under the applied force.[53–55]

We used a computer as the "electronic brain" to mimic the logic functions of the human brain and utilized the HS-CNT/LCE artificial muscle to replicate the intelligent actuation performance of a real muscle spindle as shown in Fig. 5b. In the artificial muscle system developed in the current study (Fig. 5c and Fig. S16, ESI†), we can monitor the resistance change in the HS-CNT/LCE actuator, which is similar to the excitation signal received by the nerve fibers. Simultaneously, the signal of the resistance change can be transmitted to the corresponding warning element and the power supply that provides the HS-CNT/LCE actuator with thermal energy through the Raspberry Pi and the conversion chip. By setting the thresholds of resistance change corresponding to different components, different dynamic behaviors of an artificial system can be achieved, which enables the implementation of control strategies comparable to those employed by humans.

Next, we integrated the HS-CNT/LCE actuator with a control system to mimic the control of lifting a heavy object through the human muscles. The HS-CNT/LCE actuator demonstrated varying strains and degrees of resistance change when different

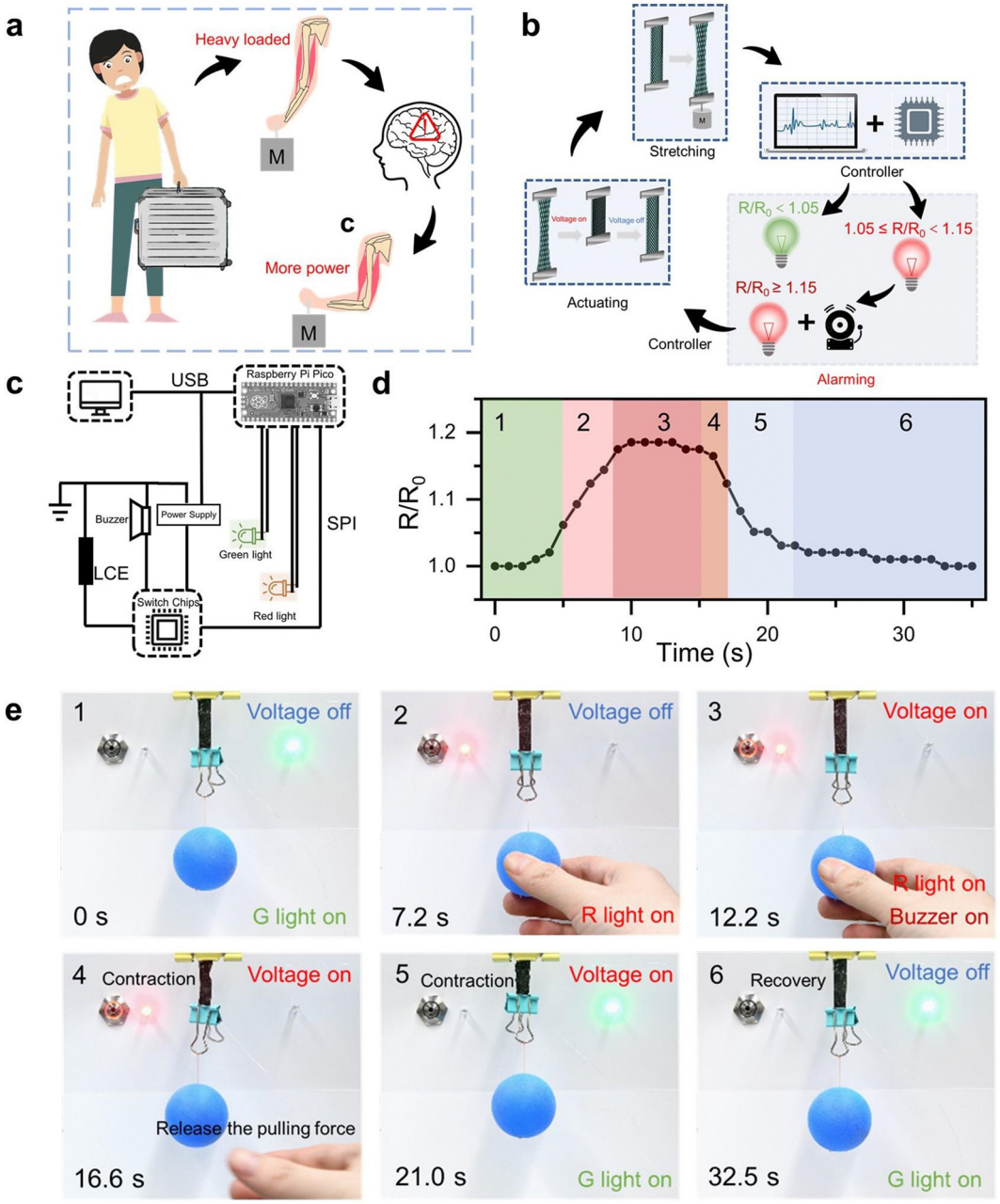

Fig. 5 Closed-loop control system. (a) Schematics showing humans lifting heavy loads: when the lifted object is too heavy, the central nervous system sends a command for the muscles to output more force. (b) Schematic diagram of the closed-loop control artificial muscle system based on the HS-CNT/LCE actuator. (c) Biomimetic circuit design of the closed-loop control for the intelligent artificial muscle system. (d) Resistance changing curve of the HS-CNT/LCE actuator during the stretching process in the system. (e) Experimental photographs showing the real-muscle-like morphing intelligence of the HS-CNT/LCE artificial muscle.

weights of heavy objects were hung (Fig. S17 and S18, ESI†). Manual stretching of the HS-CNT/LCE actuator resulted in the system behavior shown in Fig. 5e (Movie S4, ESI†). When a weight of 2 g was hung, the resistance of the HS-CNT/LCE actuator remained relatively constant, indicated by the constant green light. However, when the actuator was stretched downward, the resistance gradually increased, as illustrated in Fig. 5d. At a certain stretch ratio where the resistance changed by more than 5%, the green light turned off and the red light remained illuminated. Further stretching resulted in resistance changes exceeding 10%, triggering the activation of the red light and the sounding of the buzzer. Simultaneously, a pre-programmed voltage (V = 4 V and t = 5 s) was sent to trigger the contraction of the HS-CNT/LCE actuator. Upon release of the pulling force, the contraction deformation of the film became evident, and the resistance returned to its initial state, accompanied by the cessation of the buzzer. Subsequently, the red light turned off and the green light turned on. This closed-loop

control based on the HS-CNT/LCE endows the artificial muscles with enhanced intelligence during the operation process. By emulating the natural responses and control mechanisms observed in biological systems, our smart artificial muscle system exhibits promising potential for a wide range of applications.

3. Conclusion

In conclusion, we created conceptually new hierarchically structured HS-CNT/LCE composite artificial muscles enabling the unique combination of omnidirectionally-tunable stretchability, stable electro-mechanical actuation during large deformation, low-voltage driving, large actuation strain, powerful actuation, and long-term working stability, which has been proved extremely difficult to achieve in existing electromechanical artificial muscles. In our hierarchically structured artificial muscles, aligned CNT networks offer directionally-stretchable/deformable functions while randomly oriented CNT networks provide omnidirectional large-scale stretchability/deformation without compromising electro-thermal stability and mechanical output power. Furthermore, coupled with electronic control components, a closed loop of sense and actuation can be built in our artificial muscles to enable remarkable autonomous and adaptive real-muscle-like intelligence (*e.g.*, self-monitoring, self-alarming, and self-healing). It is anticipated that the development of such HS-CNT/LCE composite artificial muscles would promise immense benefits for the advances in the fields that urgently need high-performance electro-mechanical soft actuators.

Experimental section

Materials

RM82 (1,4-bis-[4-(6-acryloyloxyhexyloxy)benzoyloxy]-2-methylbenzene) was purchased from Shijiazhuang Yesheng Chemical Technology Co., Ltd. DODT (3,6-dioxa-1,8-octanedithiol), pentaerythritol tetrakis (3-mercaptopropionate) (PETMP) and dipropylamine (DPA, 99%) were obtained from TCI. Single-walled carbon nanotubes (SWCNTs, 93%) were provided by OCSiAl company. The chlorosulfonic acid (99%) was obtained from Shanghai Xianding Biotechnology Co., Ltd.

Fabrication of bilayer HS-CNT/LCE composite films

The superacid slide coating method for HS-CNT film fabrication: 3 mL of chlorosulfonic acid (99%) was added to a certain mass (14 mg or 56 mg) of SWCNTs and stirred vigorously for 3 days inside a glove box filled with nitrogen. A drop of the prepared SWCNT ink was sandwiched between two glass slides. The two slides were rapidly slid across each other in opposite directions, producing a HS-CNT film on each glass slide. Each slide was dried slowly in an inert atmosphere to remove any acid leached out of the film.

The HS-CNT/LCE film fabrication method: a mixture was formulated with 1.92 : 1 molar ratio of RM82 and DODT, 3 : 1 molar ratio of DODT:PETMP, and 0.1 wt% photoinitiator I-651. The molar ratio of thiol groups to acrylate groups is 1 : 1.15. The mixture was dissolved in chloroform. After ultrasonic dispersion of 4 h, a catalytic amount of DPA was added to the solution. As shown in Fig. S1 (ESI†), the mixture containing 400 mg RM82 was transferred into a custom-made glass mold (3 cm × 5 cm × 1 cm) quickly. The loosely crosslinked LCE film formed after 30 min at room temperature. The formed film was pre-stretched and laminated on the top of the HS-CNT film and held at 10 N pressure for 12 h to achieve the HS-CNT/LCE film. Finally, a monodomain HS-CNT/LCE film was obtained by exposing it to 365 nm UV (10 mW cm^{-2}) for 10 min. The prestretch λp is defined as the ratio of the length of the monodomain films to the initial length of the polydomain films. If not otherwise specified, the prestretch λp is 150%.

Characterization

An analytical field emission scanning electron microscope (Gemini450) was used at 3 kV to examine the morphologies of HS-CNT films prepared from different concentrations of the superacid dispersion under different stretching strains and angles. A DC power source (ITECH 6332A) was used to provide the heating power. The surface temperature of the actuator was measured using an infrared thermometer (A665sc, FLIR). The photographs and videos were recorded with a digital camera (Canon, EOS 80D(W)). DSC thermograms were obtained using a TA Discovery DSC 250 (Rate of heating: 5 °C min^{-1}, N_2 flow 50 mL min^{-1}). Thermogravimetric analysis (TGA) was carried out on a Mettler-Toledo TGA/DSC 3+/1600 HT analyzer. The mechanical properties and actuation stress of the HS-CNT/LCE actuators were investigated using an Instron 5943 universal testing system. Electrical performance was investigated using an electrochemical workstation (Zennium pro/Reference 600+&Spectro-115U), a multimeter (FLUKE 107), and a power source (ITECH 6332A).

Conflicts of interest

The authors declare no competing interests.

Acknowledgements

This research was supported by the National Natural Science Foundation of China (52273111, 62204208), the Natural Science Foundation of Zhejiang Province of China (LR22E030004), and the Foundation of Westlake University.

References

1 M. Li, A. Pal, A. Aghakhani, F. A. Pena and M. Sitti, *Nat. Rev. Mater.*, 2021, **7**, 235.
2 Y. S. Zhao, C. Y. Lo, L. C. Ruan, C. H. Pi, C. Kim, Y. Alsaid, I. Frenkel, R. Rico, T. C. Tsao and X. M. He, *Sci. Rob.*, 2021, **6**, 5483.

3 J. K. Sun, W. J. Guo, G. K. Mei, S. L. Wang, K. Wen, M. L. Wang, D. Y. Feng, D. Q. Qian, M. F. Zhu, X. Z. Zhou and Z. F. Liu, *Adv. Mater.*, 2023, **35**, 2212112.
4 A. Q. Khan, K. Q. Yu, J. T. Li, X. Q. Leng, M. L. Wang, X. S. Zhang, B. G. An, B. Fei, W. Wei, H. C. Zhuang, M. Shafiq, L. L. Bao, Z. F. Liu and X. Zhou, *Adv. Fiber Mater.*, 2022, **4**, 1572–1583.
5 B. Cui, M. Ren, L. Z. Dong, Y. L. Wang, J. F. He, X. L. Wei, Y. R. Zhao, P. P. Xu, X. N. Wang, J. T. Di and Q. W. Li, *ACS Nano*, 2023, **17**, 12809–12819.
6 M. T. Li, Y. C. Tang, R. H. Soon, B. Dong, W. Q. Hu and M. Sitti, *Sci. Adv.*, 2022, **8**, eabm5616.
7 W. H. Hou, J. Wang and J. A. Lv, *Adv. Mater.*, 2023, **35**, 2211800.
8 D. S. Wu, Y. N. Zhang, H. R. Yang, A. F. Wei, Y. X. Zhang, A. Mensah, R. Yin, P. F. Lv, Q. Feng and Q. F. Wei, *Mater. Horiz.*, 2023, **10**, 2587–2598.
9 Y. P. Wang, J. H. Sun, W. Liao and Z. Q. Yang, *Adv. Mater.*, 2022, **34**, 2107840.
10 L. Chen, Y. L. Zhang, K. H. Zhang, F. Li, G. G. Duan, Y. Sun, X. H. Wei, X. X. Yang, F. Wang, C. M. Zhang, S. S. Li, X. Y. Cao, C. X. Ma and S. H. Jiang, *Chem. Eng. J.*, 2023, **480**, 148205.
11 Q. G. He, Z. J. Wang, Y. Wang, A. Minori, M. T. Tolley and S. Q. Cai, *Sci. Adv.*, 2019, **5**, eaax5746.
12 H. E. Fowler, P. Rothemund, C. Keplinger and T. J. White, *Adv. Mater.*, 2021, **33**, 2103806.
13 S. M. Mirvakili and I. W. Hunter, *Adv. Mater.*, 2018, **30**, 1704407.
14 R. H. Baughman, *Synth. Met.*, 1996, **78**, 339–353.
15 L. Hines, K. Petersen, G. Z. Lum and M. Sitti, *Adv. Mater.*, 2017, **29**, 1603483.
16 M. Farid, Z. Gang, T. L. Khuong, Z. Z. Sun, N. Ur. Rehman and M. Rizwan, *J. Biomimetics, Biomater. Biomed. Eng.*, 2014, **20**, 1–10.
17 R. K. Cheedarala, J. H. Jeon, C. D. Kee and I. K. Oh, *Adv. Funct. Mater.*, 2014, **24**, 6005–6015.
18 S. Ahn, R. M. Kasi, S. C. Kim, N. Sharma and Y. Zhou, *Soft Matter*, 2008, **4**, 1151–1157.
19 M. Z. Uddin, M. Watanabe, H. Shirai and T. Hirai, *J. Polym. Sci., Part B. Polym. Phys.*, 2003, **41**, 2119–2127.
20 Z. M. Hu, Y. L. Li and J. A. Lv, *Nat. Commun.*, 2021, **12**, 3211.
21 Z. C. Guan, L. Wang and J. Bae, *Mater. Horiz.*, 2022, **9**, 1825–1849.
22 J. Z. Zhang, D. D. Sun, B. Zhang, Q. Q. Sun, Y. Zhang, S. R. Liu, Y. M. Wang, C. T. Liu, J. Z. Chen, J. B. Chen, Y. L. Song and X. Y. Liu, *Mater. Horiz.*, 2022, **9**, 1045–1056.
23 Y. Chen, H. Zhao, J. Mao, P. Chirarattananon, E. F. Helbling, N.-S. P. Hyun, D. R. Clarke and R. J. Wood, *Nature*, 2019, **575**, 324–329.
24 E. Hajiesmaili, Na. M. Larson, J. A. Lewis and D. R. Clarke, *Sci. Adv.*, 2022, **8**, eabn9198.
25 Q. Pei, M. Rosenthal, S. Stanford, H. Prahlad and R. Pelrine, *Smart Mater. Struct.*, 2004, **13**, N86.
26 X. B. Ji, X. C. Liu, V. Cacucciolo, Y. Civet, A. E. Haitami, S. Cantin, Y. Perriard and H. Shea, *Adv. Funct. Mater.*, 2021, **31**, 2006639.
27 Y. Guo, L. Liu, Y. Liu and J. Leng, *Adv. Intell. Syst.*, 2021, **3**, 2000282.
28 Y. H. Wang, X. Z. Ma, Y. J. Jiang, W. P. Zang, P. F. Cao, M. Tian, N. Y. Ning and L. Q. Zhang, *Res. Chem. Mater.*, 2022, **1**, 308–324.
29 W. Lehmann, H. Skupin, C. Tolksdorf, E. Gebhard, R. Zentel, P. Krüger, M. Lösche and F. Kremer, *Nature*, 2001, **410**, 447–450.
30 T. Mirfakhrai, J. D. W. Madden and R. H. Baughman, *Mater. Today*, 2007, **10**, 30–38.
31 Y. Wang, Q. G. He, Z. J. Wang, S. J. Zhang, C. H. Li, Z. J. Wang, Y. L. Park and S. Q. Cai, *Adv. Mater.*, 2023, **35**, 2211283.
32 A. Kotikian, J. M. Morales, A. Lu, J. Mueller, Z. S. Davidson, J. W. Boley and J. A. Lewis, *Adv. Mater.*, 2021, **33**, 2101814.
33 J. H. Sun, Y. P. Wang, W. Liao and Z. Q. Yang, *Small*, 2021, **17**, 2103700.
34 Y. Y. Xiao, Z. C. Jiang, X. Tong and Y. Zhao, *Adv. Mater.*, 2019, **31**, 1903452.
35 H. R. Liu, H. M. Tian, J. Y. Shao, Z. J. Wang, X. M. Li, C. H. Wang and X. L. Chen, *ACS Appl. Mater. Interfaces*, 2020, **12**, 56338–56349.
36 L. M. Zhao, H. M. Tian, H. R. Liu, W. T. Zhang, F. B. Zhao, X. W. Song and J. Y. Shao, *Small*, 2023, **19**, 2206342.
37 X. K. Li, Y. Jung, K. Sakimoto, T. H. Goh, M. A. Reedbc and A. D. Taylor, *Energy Environ. Sci.*, 2013, **6**, 879–887.
38 L. H. Jin, A. Chortos, F. F. Lian, E. Pop, C. Linder, Z. N. Bao and W. Cai, *Proc. Natl. Acad. Sci. U. S. A.*, 2018, **115**, 1986–1991.
39 X. P. Han, Y. Huang, J. M. Wang, G. Z. Zhang, T. H. Li and P. B. Liu, *Composites, Part B*, 2022, **229**, 109458.
40 Y. P. Jia, R. Z. Sun, Y. Pan, X. Wang, Z. Y. Zhai, Z. Y. Min, G. Q. Zheng, C. T. Liu, C. Y. Shen and X. H. Liu, *Composites, Part B*, 2021, **210**, 108668.
41 X. L. Chen, S. H. Nie, W. R. Guo, F. Fei, W. M. Su, W. B. Gu and Z. Cui, *Adv. Electron. Mater.*, 2019, **5**, 1800991.
42 H. Kim, M. Seo, J. W. Kim, D. K. Kwon, S. E. Choi, J. W. Kim and J. M. Myoung, *Adv. Funct. Mater.*, 2019, **29**, 1901061.
43 X. He, G. Z. Shen, R. B. Xu, W. J. Yang, C. Zhang, Z. H. Liu, B. H. Chen, J. Y. Liu and M. X. Song, *Polymers*, 2019, **11**, 468.
44 W. W. Li, M. Sang, S. Liu, B. C. Wang, X. F. Cao, G. H. Liu, X. L. Gong, L. Y. Hao and S. H. Xuan, *Composites, Part B*, 2022, **238**, 109880.
45 K. F. Wang, C. Chen, Q. T. Zheng, J. Xiong, H. Z. Liu, L. Yang, Y. J. Chen and H. Li, *Carbon*, 2022, **197**, 87–97.
46 J. J. Wu, M. X. Wang, L. Dong, J. Shi, M. Ohyama, Y. Kohsaka, C. H. Zhu and H. Morikawa, *ACS Nano*, 2022, **16**, 12801–12812.
47 Y. F. Cui, Z. Jiang, G. L. Zheng, W. D. Wang, M. Zhou, P. Wang, Y. Y. Yu and Q. Wang, *Chem. Eng. J.*, 2022, **446**, 137189.
48 Y. Liao, Y. F. Tian, X. H. Ma, M. J. Zhao, J. Qian and X. Wang, *ACS Appl. Mater. Interfaces*, 2020, **12**, 48077–48083.
49 W. Chen, S. Q. Yang, H. T. Wang, K. T. Yang, X. L. Wu, F. Gao, B. J. Zheng, K. Qian, W. Yao, T. Zhang, B. Zhong and X. X. Huang, *Chem. Eng. J.*, 2022, **431**, 133990.
50 B. Zhou, X. Q. Han, L. Li, Y. Z. Feng, T. Fang, G. Q. Zheng, B. Wang, K. Dai, C. T. Liu and C. Y. Shen, *Compos. Sci. Technol.*, 2019, **183**, 107796.

51 C. P. Sharma and C. J. Arnusch, *Carbon*, 2022, **196**, 102–109.
52 L. H. Li, S. K. Hong, Y. Jo, M. D. Tian, C. Y. Woo, S. H. Kim, J. M. Kim and H. W. Lee, *ACS Appl. Mater. Interfaces*, 2019, **11**, 16223–16232.
53 J. L. Taylor, J. E. Butler and S. C. Gandevia, *Eur. J. Appl. Phys.*, 2000, **83**, 106–115.
54 S. C. Gandevia, *Physiol. Rev.*, 2001, **81**, 1725.
55 S. Erimaki and C. N. Christakos, *J. Neurophysiol.*, 1999, **82**, 2839–2846.